Pre-print of a published manuscript

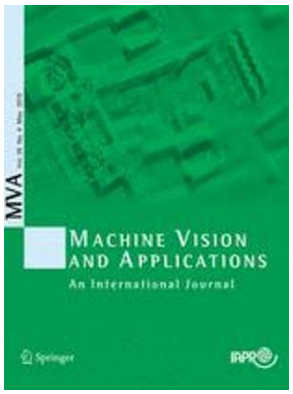

Automating shockwave segmentation in low-contrast coherent shadowgraphy

Jaka Pribošek, Peter Gregorčič, Janez Diaci

DOI: https://doi.org/10.1007/s00138-015-0683-0
Published in: Machine Vision and Applications, May 2015, Volume 26, Issue 4, pp 485–494

Received: 17 February 2015
Accepted: 12 August 2015

This is a pre-print of an article published in Machine Vision and Applications. The final authenticated version is available online at: https://doi.org/10.1007/s00138-015-0683-0.

Please cite this article as: J. Pribosek, P. Gregorcic, J. Diaci, Automating shockwave segmentation in low-contrast coherent shadowgraphy, Machine Vision and Applications, 26 (2015) 485-494, DOI: https://doi.org/10.1007/s00138-015-0683-0

Automating shockwave segmentation in low-contrast coherent shadowgraphy

Jaka Pribošek*, Peter Gregorčič, Janez Diaci

University of Ljubljana, Faculty of Mechanical Engineering

jaka.pribosek@fs.uni-lj.si

Abstract

The paper presents a method that enables automated segmentation of the low-contrast shadowgraph images, e.g., acquired in the studies of laser induced shockwave phenomena. The method is especially suitable for the analysis of large image data sets, such as obtained at studying the evolution of laser-induced shockwaves with high spatial and temporal resolution. The method comprises two active contours algorithms. First, the approximate shape of the shockwave is detected by a traditional snake algorithm using external energies that base on texture cues. The outcome of the coarse detection serves as an initialization to the second refining stage detection introducing a Greedy snake algorithm. Local optimum is searched with respect to responses of steerable filtering and edge orientation similarity by exploiting the Bayesian formalism. The paper presents validation of the method on sample of 12 low contrast shadowgraphs by comparison to the manual segmentation technique. The obtained results demonstrate overall good performance, robustness and high accuracy of the method.

Keywords: ***low-contrast segmentation, shockwave, laser-induced breakdown in air, active contours, low-contrast shadowgraphy***

1 Introduction

Studying the shockwave phenomena is of a great importance in many different areas of physics and applied sciences and finds its use in a wide spectrum of medical applications [1]. Multiple numerical and experimental studies on shockwaves, their induction mechanisms and their propagation under various circumstances have been recently demonstrated. Among those, the study of optodynamic energy-conversion efficiency [2], derivation of equations of state [3], [4] and validation of analytical and numerical models proposed by various research groups [5] are of importance for deeper understanding of shockwave physics and material science.

Over past few years, various different systems for shockwave inspection, involving Schlieren imaging technique [6], [7] and shadowgraphy [8] have been developed and used. In both techniques, the observation of transient phenomena is possible due to the variations of refractive index of the medium [9]. High contrast shadowgraphs can be obtained with set-ups where large variations in refractive index occur. This makes Schlieren and shadowgraphic techniques suitable mainly for observations of shockwaves in solids and liquids. On the other hand, extremely low contrast of shadowgraphs is encountered in experiments with gases, where the refractive-index variations are significantly smaller than in solids or liquids [10], [11]. Additionally, the pressure of the

shockwave front is fading away by propagation, which also results in lower contrast of the acquired images. This makes the observation of shockwaves in gases a challenging problem. In order to overcome these problems, improvements of existing Schlieren visualization techniques has been proposed by Vogel et al. [10] to increase the sensitivity of the imaging technique and assure images having a higher contrast. However, there is still a lack of experimental studies encountering challenging visualization and data analysis in low-contrast shadowgraphs.

Automated computer-controlled systems for laser-induced plasma and shockwave phenomena have recently been reported [8]. Such systems are fully automated and controlled by a computer, and thus have the capabilities of acquiring the shockwave phenomena autonomously. This opens a possibility of creation of large database of various shockwaves under different circumstances which is important for thorough validation of analytical and numerical models. Although the systems are fully autonomous for data acquisition, the current data processing involves manual shockwave segmentation technique [12], which remains the main reason for hindering the creation of large database. In order to alleviate this problem, we strive for automatic shock-wave segmentation based on image processing. No thorough study on image processing on laser-induced shockwaves shadowgraph can be found in the open literature. Nevertheless, for high-contrast images, many standard image processing techniques may yield good results [13]. However, these techniques are insufficient for the processing of low-contrast shadowgraphs, where high-level algorithm for image segmentation is required.

The main aim of this paper is to solve the low-contrast shadowgraph segmentation problem. For automatic shock wave segmentation in low-contrast shadowgraphs, we describe a novel two-stage, low-contrast shockwave segmentation method based on active contours.

2 A background of laser shadowgraphy

In shadowgraphy, white light seems to be a preferable choice for illumination of wide variety of applications due to its flexibility, low-cost and low-coherence yielding good image quality, i.e., high signal-to-noise ratio [9]. Here, typical pulse durations of spark gap light sources are in the range between 1–10 ns. However, very high-speed phenomena, such as plasma ignition and shockwave generation, propagate with velocities up to 600 km/s and 100 km/s, respectively [8,11]. Therefore, in these cases a very short illumination of less than 100 ps is required to achieve a spatial resolution of about 10 μm. Consequently, a short laser pulse is the only option for illumination ensuring a high spatial resolution.

A coherent-laser illumination introduces many drawbacks regarding image quality, such as the presence of noise that is caused by laser speckles and diffraction pattern, clearly visible in Figure 2A as a regular pattern of fringes. Here, Fig. 2A is acquired 132 ns after the laser breakdown in air and a 30-ps, green-laser pulse was used as an illumination source (see experimental setup in Refs. [8,11]). All these interference phenomena that appear due to the coherent illumination light are undesirable and strongly impede the image processing. From Fig. 2A it is visible that the shockwave boundary is rather

indistinctive on the low-contrast shadowgraph image hindering robustness of shockwave detection. It is therefore important to incorporate other image cues for successful detection. To do this, the understanding of image formation is crucial.

Figure 1 is depicting a shockwave illuminated by coherent light. Black dots represent the unique and static speckle pattern in the illumination which can be priory acquired as a background image (e.g., the left-hand side of Fig. 1). Once the light passes through the shock wave, the speckle pattern gets distorted and displaced behind the object due to the refractive-index gradient, as schematically presented on the right-hand side of Fig. 1. By subtracting the background from the image the speckle effect is doubled behind the object due to the light deflection and suppressed elsewhere (Fig. 2B shows a typical shadowgraph image after the background subtraction). Thus, the background subtraction improves the overall SNR and yields the important change in texture within the observed object. This way, we turn the laser speckles, often considered as undesired, into an advantage in the context of image processing.

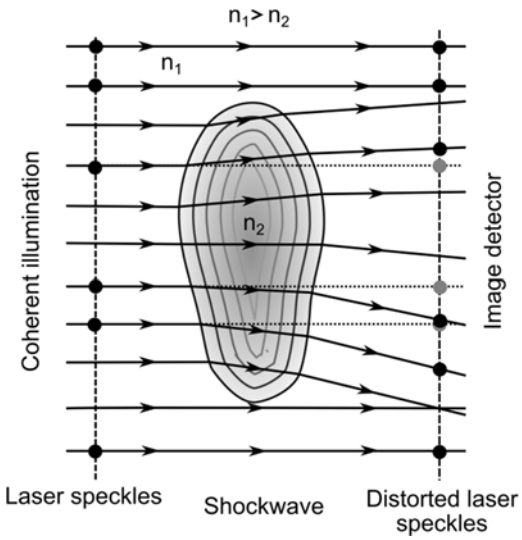

Figure 1: Distortion of the static laser speckles pattern due to the light deviation

3 Algorithm for automatic segmentation

To exploit different cues into the successful shockwave-boundary detection we propose a novel two-stage method. In the first stage, the approximate shape of the contour is detected by exploiting texture cues. This coarse detection is then followed by a refinement stage, where the contour is modified by employing the boundary information. Both stages incorporate active contour algorithms in order to detect the shockwaves.

3.1 Active contours

Snakes and active contours has been already proved as prominent methods in wide variety of applications and gain extreme attention due to their high flexibility and versatility [14], [15]. To facilitate understanding of the shock segmentation method we present here a brief overview of the active contours, i.e., snakes used hereafter. A detailed description and derivation can be found elsewhere [16][17]. Let $s(p)=\left[x(p),y(p)\right]^T$ be the coordinates of a closed contour that encircles the object of interest. Here, p stands for the parameter running along the closed contour. As proposed by Kass et al. [16], the snake energy E consists of internal, E_{int}, and external, E_{ext}, energy as:

$$E=\oint\left(E_{int}\left(s(p)\right)+E_{ext}\left(s(p)\right)\right)dp \tag{1}$$

The internal energy in eq. (1) is defined as

$$E_{int}\left(s(p)\right)=\frac{1}{2}\left(\alpha(p)\left|s'(p)\right|^2+\beta(p)\left|s''(p)\right|^2\right) \tag{2}$$

where parameter $\alpha(p)$ controls the stiffness and parameter $\beta(p)$ controls the smoothness of the snake. These two parameters are often kept constant for all contour points. In traditional snake, the external energy, E_{ext}, is often derived from the image and/or may include many other different cues that offer a flexible way of tuning the snake performance to one's need. When the snake is evolving, the external field is interpolated according to the snake's current location in order to get the current external forces that drive the snakes. Later variation of traditional snakes, called greedy snake, was introduced by Lam et al. [18]. In greedy snakes the local optimum according to some merit functions is searched for each snake point in each step of the iteration. Such approach allows to dynamically change the merit functions that offer a convenient way to make the snake adaptive. More attention to the derivation of specific external energies for our problem will be given in the following subsections.

Once both, internal and external parts of the total energy are determined, the total energy is minimized using the Euler Lagrange equation. This leads to the following expression [16], [17]:

$$\alpha(p)s''(p)-\beta s^{(4)}(p)-\nabla E_{ext}\left(s(p)\right)=0 \tag{3}$$

Equation (3) is solved iteratively with gradient descent method as proposed by Kass et al. [16] using a finite difference approximation of the spatial derivatives.

3.2 Coarse detection

Before the image processing, the pre-acquired background image is firstly subtracted from every upcoming image in order *(i)* to increase the contrast between the object of interest, and *(ii)* to generate the texture differences, as described in section 2. As evident in Figure 2B, the diffraction pattern remains remain visible after background subtraction. In order to avoid its influence on segmentation, our algorithm bases entirely on the textures. The texture difference is clearly revealed after the nonlinear image filtering, that it is achieved by calculation of the image variance in region of 3x3 pixels (Figure 2C). This allows the direct construction of the external energy gradient required for active contour formulation, as in eq.(3). Since we know that the object appears approximately in the center of the image $[x_c, y_c]$, we define the external energy gradient at each pixel $[x, y]$ that points either towards or outwards the center and has a magnitude proportional to image intensity drawn from the variance image I_{var}

$$\nabla E_{ext}(x,y) = \begin{cases} -I_{\mathrm{var}} \dfrac{\vec{v}}{\|\vec{v}\|} & ;\ I_{var} \geq I_{thresh} \\ \left(1 - I_{\mathrm{var}}\right) \dfrac{\vec{v}}{\|\vec{v}\|} & ;\ I_{var} < I_{thresh}, \end{cases} \tag{4}$$

where $\vec{v} = [x - x_c, y - y_c]$ and I_{thresh} defining a threshold value, which decides whether the vector at some location pushes the snake towards the center or repels it away from the center. A very basic version of the snake algorithm is then launched by using this external energy gradient. The snake is initialized by an elliptic region, which is placed at the center of the image. By setting the I_{thresh}, the snake is converging fast and yields good approximations to the shockwave contour. Once reaching the boundaries of the shockwave, the snake does not converge smoothly to the final contour but instead becomes shaky and unstable, owing to the unsmooth nature of external field definition. Such unsmooth external field is proved to be welcome in order to enable quick jumps in snake position and shape, hoping for fast and robust energy minimization. However, we strive to ensure the snake convergence and to achieve this completely we have to moderate the shakiness. To do this, we linearly decrease the amplitude of the external field to stabilize the snake until convergence is reached. This requires only few additional iterations. Once the convergence is reached, we resample the snake equidistantly along the contour in order to release snakes inner energies for initialization of the refinement stage. By testing various different algorithms, this snake-based texture-segmentation has been found superior in performance in comparison with other segmentation techniques that we also tried, e.g., binarization, morphological filtering or Markov Random Field segmentation.

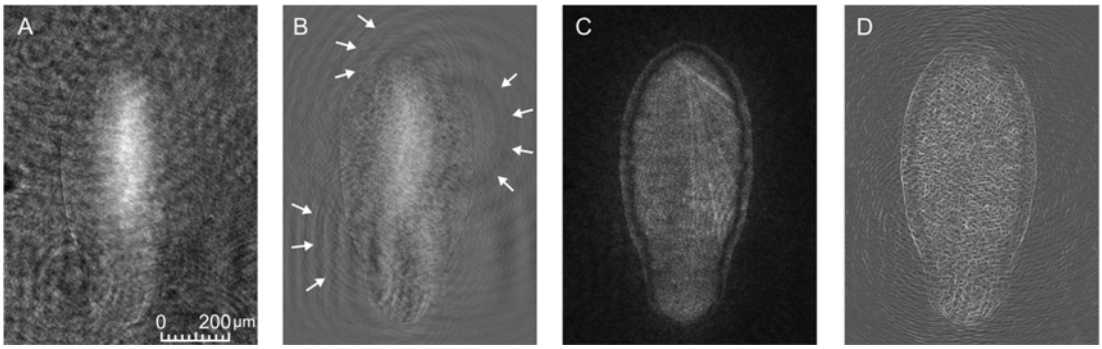

Figure 2: A: original image, B) image after background subtraction with arrows indicating the diffraction pattern, C) Texture image, D) Detected boundaries

3.3 Fine segmentation

The extracted contour, obtained with the coarse detection stage, is close to desired shock contour, however, a local refinements are still necessary. For this purpose we use the Greedy-snake approach [18], where the contour is locally optimized to the shockwave boundary. Since the contrast at the edges of the shockwave is low and the edge is thin, classic gradient-based-edge detection yields poor results. In the literature, Hessian ridge detector is often applied for this task [19]. We use steerable filters [20] in order to detect ridges and extract their orientation. Here, we employ the Laplacian of Gaussian filters at three different scales. At each scale, the filters are oriented at six different orientations. $\theta = \{0,\ \pi/6, \pi/3, \pi, 2\pi/3, 5\pi/6\}$. By deriving the anisotropic Laplacian of Gaussian and introducing the coordinate rotation by an angle θ, we end up with:

$$G(\sigma_u, \sigma_v, \theta) = -\frac{1}{2\pi\sigma_u\sigma_v}\left(-\frac{1}{\sigma_u^2}-\frac{1}{\sigma_v^2}-\frac{\left(x\cos\theta+y\sin\theta\right)^2}{\sigma_u^4}-\frac{\left(-x\sin\theta+y\cos\theta\right)^2}{\sigma_v^4}\right)$$
$$\exp\left\{-\frac{1}{2}\left(\frac{\left(x\cos\theta+y\sin\theta\right)^2}{\sigma_u^2}+\frac{\left(-x\sin\theta+y\cos\theta\right)^2}{\sigma_v^2}\right)\right\} \quad (5)$$

Figure 3 shows the filter bank that was calculated by eq. (5) using the parameters described above.

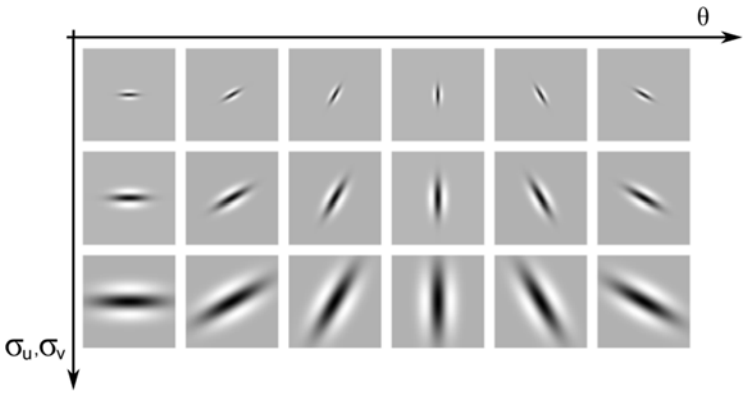

Figure 3: Steerable filters calculated by eq. (5).

Convolving the input image with steerable filters yields high responses at the thin black outline of the shock wave as shown in Figure 2D. For efficient implementation to avoid the high computation costs, all convolutions were implemented by the use of Fourier transform. The filtered $I(\sigma_u, \sigma_v, \theta)$ is then given as:

$$I(\sigma_u, \sigma_v, \theta) = \mathcal{F}^{-1}\left\{\mathcal{F}\{I\}\,\mathcal{F}\left\{G(\sigma_x, \sigma_y, \theta)\right\}\right\} \tag{6}$$

where $\mathcal{F}\{\}$ and $\mathcal{F}^{-1}\{\}$ denote the Fourier transform and its inverse respectively. The image of detected boundaries (Figure 2D) is determined by taking the maximum filter response at each pixel location. The orientation of this edge is drawn from the filter orientation θ that yields that response.

$$\begin{aligned} I_{edge} &= \max\left(I(\sigma_u, \sigma_v, \theta)\right) \\ \theta_{edge} &= \arg\max_{\theta}\left(I(\sigma_u, \sigma_v, \theta)\right) \end{aligned} \tag{7}$$

Following the idea of Radeva et.al [21] that the snake should be attracted only to high level edges with similar orientation to the snake tangent, we introduce the Bayesian formalism in order to combine boundary and orientation cues to a robust high-level detection. Boundary likelihood $p(y_{bound} \mid \mathbf{x})$ for a given position on the image $\mathbf{x} = [x, y]$ is constructed by simply normalizing the I_{edge}. In order to construct the orientation likelihood $p(y_{orient} \mid \mathbf{x})$, the orientation θ_{edge} is compared to the tangent orientation of the snake at every iteration. Orientation similarity measure is introduced for this task. Given the snake contour, the tangent angle at every node of contour is calculated by:

$$\psi = \operatorname{atan} 2(\dot{y}, \dot{x}) \tag{8}$$

$$\psi_{ref} = \begin{cases} \psi & ;\psi \le 0 \\ \psi + \pi & ;\psi > 0 \end{cases} \tag{9}$$

where atan2() is the arctangens function defined on all four quadrants.

For similarity measure, a cosine function is introduced in order to weight edges with similar orientation to the starting curve and suppress edges with perpendicular orientation. The orientation likelihood is thus formulated as:

$$p\left(y_{orient} \mid \mathbf{x}\right) = \frac{1}{2}\left|\cos\left(\theta_{edge} - \psi_{ref}\right)\right| + \frac{1}{2} \tag{10}$$

Search of local optimum is accomplished by the Bayesian formalism. We want to combine the orientation likelihood $p\left(y_{orient} \mid \mathbf{x}\right)$ with boundary likelihood $p\left(y_{bound} \mid \mathbf{x}\right)$ in order to improve the detection. Assuming both likelihoods are independent, their joint likelihood can be formulated as:

$$\begin{aligned} p\left(y_{joint} \mid \mathbf{x}\right) &= p\left(y_{orient}, y_{bound} \mid \mathbf{x}\right) \\ p\left(y_{orient}, y_{bound} \mid \mathbf{x}\right) &= p\left(y_{orient} \mid \mathbf{x}\right) p\left(y_{bound} \mid \mathbf{x}\right) \end{aligned} \tag{11}$$

To make overall tracking with the use of the combined probability density functions less prone to failure, the modified 2D Epanechnikov kernel [22] is superimposed over the joint likelihood. This gives more weight to locations near current snake position and less to more distant one. The final joint likelihood can be then seen in Figure 4C Local maxima of the joint probability, the so called Maximum A Posteriori (MAP), depicted with red cross in the Figure 4C, is then used as the next most possible location x_{map}

$$x_{map} = \max_{x}\left(p\left(y_{orient}, y_{bound} \mid \mathbf{x}\right)\right) \tag{12}$$

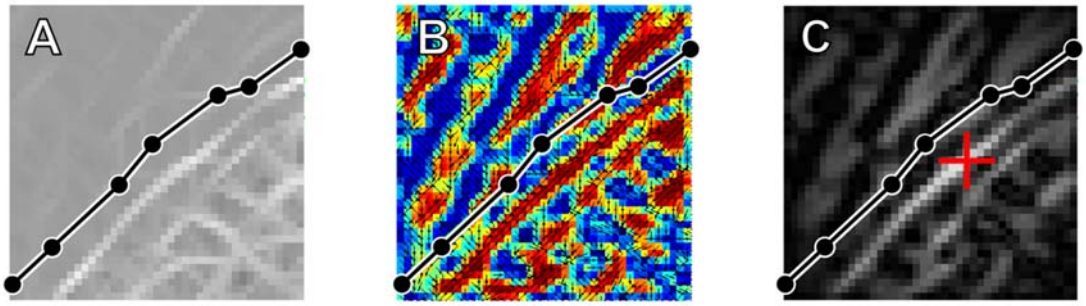

Figure 4: Greedy search algorithm : A) Boundary likelihood with initial contour B): Orientation similarity coded with color temperature, C) Joint likelihood with red cross representing the detected local optimum

Once the local optimum for each snake's node $s(p)$ has been determined, the snake is attracted to them. This procedure is iterated few times in order to obtain the global optimum of the snake's energy. Performance of the proposed scheme has been found sufficient for the cases where shockwave boundaries are continuous, smooth and visible. However, this is not the case in some parts of our shadowgraphic results. As is clearly visible from Fig. 2A, in our case the edge responses at upper and lower caps of the shockwave are weak with undeterminable orientation. This results in weak or erroneous external energies (red springs in close-up window of Figure 5). In such situations internal energies undertake the control of the snake's shape which often yields unsatisfactory

results as depicted with dotted line in close up window of Figure 5. To alleviate this problem, we propose an improvement of presented greedy snake algorithm, by introducing additional external forces at both upper and lower parts of the curve (blue springs in Figure 5).

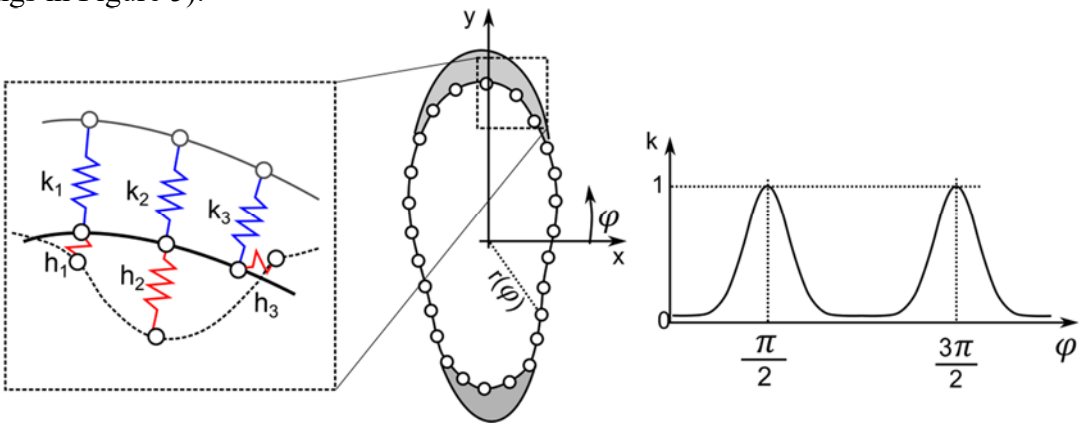

Figure 5: Extension springs compensate external energies of Greedy snake. Left: the red springs span between evolving snake and corresponding local maximum, while the blue springs span back to the texture based snake. Right: the amplitude of the blue springs according to the angular position.

The forces act as extension springs pulling the evolving snake towards to the initial texture snake. The stiffness of the springs $k(\varphi)$ is given with superimposing two normalized Gaussian functions that have their centers at $\pi/2$ and $3\pi/2$, respectively (e.g., see Figure 5c). Thus, the external force of the *p*-th node can be defined as:

$$F_{MAP} = \max\left(p\left(y_{orient}, y_{bound} \mid x\right)\right) \| s_{evolv}(p) - x_{map}(p) \| \tag{13}$$

$$F_{prior} = k(\varphi) \| s_{init}(p) - s_{evolv}(p) \| \tag{14}$$

The external energy is then formulated as a sum of the force towards local maxima F_{MAP} and prior force F_{prior} in no-contrast region. This way, the driving of the snake by sole internal energies or erroneous external energies is prevented. Final algorithm of the proposed segmentation technique is depicted in the semioperating scheme in Fig. 6.

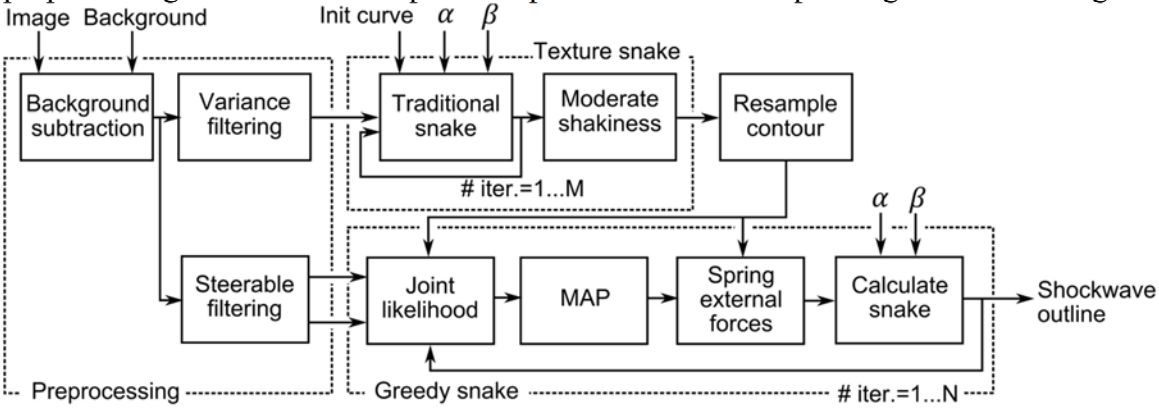

Figure 6: Two stage snake algorithm

4 Results and discussion

The proposed algorithm has been implemented and optimized in Mathworks Matlab. The size of the acquired images is 1392x1040 pixels, and the snake is initialized with the elliptical region with horizontal and vertical semi-axis being 450 pix and 650 pix, respectively. The snake comprises of 80 equidistant points along the curve. The proposed algorithm is empirically optimized and tuned to its best performance. Good performance has been generally achieved with stiffer snake. The internal energy is then somewhat lowered in the refinement stage for a more detailed contour (lower β). Final settings of the snake are represented in Table 1.

Table 1: Snake settings

Detection	Iterations	α	β
Coarse	25	0.01	0.08
Fine	25	0.01	0.07

Figure 7 shows the iteration steps in both coarse (first row) and fine stages of detection (second row). As evident, the snake converges fast and outlines the contour approximately within the coarse stage of detection. In the refinement stage, its shape is altered to better match the shockwave boundaries.

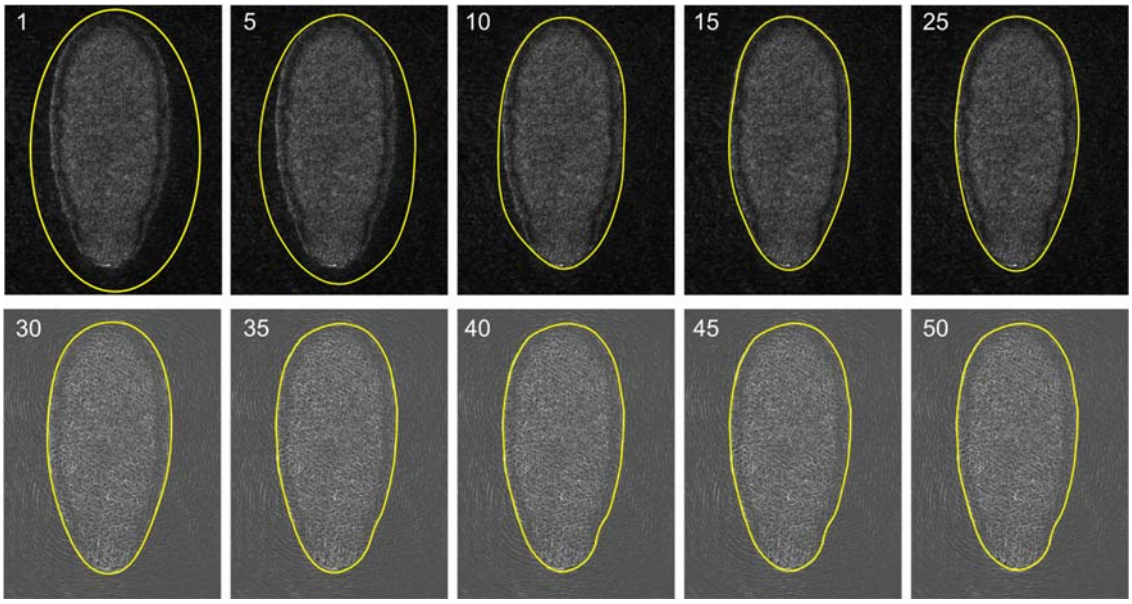

Figure 7: Coarse (1-25) and fine stage (30-50) of segmentation of shockwave Nr.5

The method has been verified on a data set of 12 shock waves, comparing the (snake) contours obtained by the automatic detection to the corresponding reference contours detected manually. The reference contours are obtained by manually selecting the node

points and interpolating them with a B-spline, as described in [12]. All contours are equiangularly sampled and transformed to polar coordinates [r, φ] with origin placed at the center of the image. This way, the discrepancy between the snake and the corresponding reference contour is estimated by observing the difference in radius $r(\varphi)$. Discrepancies are observed after both coarse and fine stages of segmentation. Table 2 presents the results. The coarse detection enables determination of shock boundary with an (RMS) error margin of about 4.6 pix. The improvement by the fine detection is significant: the error margin is reduced almost by a factor of two: to about 2.6 pix.

Figure 8 presents the absolute radius-error along the curve for both stages of detection for the shockwave Nr. 5 from Table 2. The highest errors occur at both upper and lower cap of the shockwave at $\pi/2$ and $3\pi/2$ respectively being under 15 pix for all 12 segmented shockwaves, while for the rest of the curve, the error remains under 2 pixels (Figure 8).

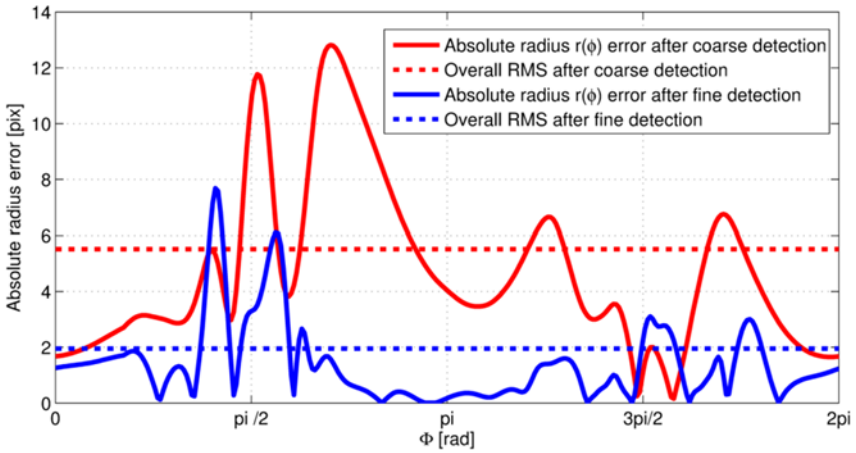

Figure 8: Absolute error after coarse and fine detection for shockwave Nr.3

Table 3 presents the results of final detection for the dataset of all 12 shockwaves, and shows good performance in comparison to manual segmentation technique. It should be highlighted, that low contrast and the presence of diffraction lobes seriously hinders the human perception. Manual segmentation is therefore not an easy task and may in many cases depend on operator interpretation. Taking this fact into account, we find the automatic segmentation method accurate and very robust.

Table 2: Results of complete detection

	Coarse detection	Fine detection				
	RMS [pix]	RMS [pix]	Min [pix]	Max [pix]	25-Percentile [pix]	75-percentile [pix]
1	4,4	1,86	-4,67	6,89	0,01	1,44
2	4,74	3,02	-3,33	11,6	-0,89	2,23
3	5,52	1,95	-7,68	6,11	-1,08	1,01
4	5,76	2,51	-9,76	5,86	-0,3	1,51
5	4,83	2,97	-2,34	11,53	-0,75	1,49
6	4,13	2,43	-5,38	11,36	-0,95	1,13
7	4,15	2,68	-4,24	12,73	-0,98	1,18
8	4,19	2,48	-4,99	8,44	-0,11	2,11
9	3,77	2,83	-5,00	12,2	-0,59	2,18
10	5,27	3,22	-5,83	10,01	-0,31	1,77
11	4,06	3,33	-3,13	9,82	-0,27	3,41
12	4,24	2,06	-5,33	6,21	-0,56	1,45
Average	**4,59**	**2,61**	**-5,14**	**9,39**	**-0,56**	**1,74**

5 Conclusions

With the presented two-stage, active-contour-segmentation method we demonstrate a practicable solution for three common problems that occur in evaluation of laser shadowgraphs of weak shock phenomena in gases: (i) diffraction patterns, (ii) general lack of image contrast, and (iii) laser speckles. By exploiting different image cues, textures and boundaries, the method enables fast, robust and accurate detection of the shockwave boundary. The performance of the algorithms has been evaluated on a sample of 12 manually segmented reference images. The method opens the way to the analysis of large datasets and thus opens new prospects for the examination of laser-induced shockwaves. Large datasets will enable additional improvements regarding the image processing by incorporation of higher lever statistics, such as active shape models.

6 Literature

[1] M. Thiel, M. Nieswand, and M. Dörffel, “The use of shock waves in medicine--a tool of the modern OR: an overview of basic physical principles, history and research,” *Minim. Invasive Ther. Allied Technol. MITAT Off. J. Soc. Minim. Invasive Ther.*, vol. 9, no. 3–4, pp. 247–253, 2000.

[2] J. Diaci and J. Možina, “Measurement of energy conversion efficiency during laser ablation by a multiple laser beam deflection probe,” *Ultrasonics*, vol. 34, no. 2, pp. 523–525, 1996.

[3] S. Chaurasia, P. Leshma, S. Tripathi, C. G. Murali, D. S. Munda, S. M. Sharma, S. Kailas, N. K. Gupta, and L. J. Dhareshwar, “Simultaneous measurement of particle velocity and shock velocity for megabar laser driven shock studies.”

[4] M. Koenig, B. Faral, J. M. Boudenne, D. Batani, A. Benuzzi, S. Bossi, C. Remond, J. P. Perrine, M. Temporal, and S. Atzeni, “Relative consistency of equations of state by laser driven shock waves,” *Phys. Rev. Lett.*, vol. 74, no. 12, p. 2260, 1995.

[5] W. Lauterborn and A. Vogel, “Shock Wave Emission by Laser Generated Bubbles,” in *Bubble Dynamics and Shock Waves*, Springer, 2013, pp. 67–103.

[6] J. Noack and A. Vogel, “Single-shot spatially resolved characterization of laser-induced shock waves in water,” *Appl. Opt.*, vol. 37, no. 19, pp. 4092–4099, 1998.

[7] H. Kleine and H. Grönig, “Color schlieren methods in shock wave research,” *Shock Waves*, vol. 1, no. 1, pp. 51–63, Mar. 1991.

[8] P. Gregorčič and J. Možina, “High-speed two-frame shadowgraphy for velocity measurements of laser-induced plasma and shock-wave evolution,” *Opt. Lett.*, vol. 36, no. 15, pp. 2782–2784, 2011.

[9] G. S. Settles, *Schlieren and shadowgraph techniques: visualizing phenomena in transparent media*. Berlin; New York: Springer, 2001.

[10] A. Vogel, I. Apitz, S. Freidank, and R. Dijkink, “Sensitive high-resolution white-light Schlieren technique with a large dynamic range for the investigation of ablation dynamics,” *Opt. Lett.*, vol. 31, no. 12, pp. 1812–1814, 2006.

[11] T. Perhavec and J. Diaci, “A novel double-exposure shadowgraph method for observation of optodynamic shock waves using fiber-optic illumination,” *Stroj. Vestn.-J. Mech. Eng.*, vol. 56, no. 7–8, pp. 477–482, 2010.

[12] P. Gregorčič, J. Diaci, and J. Možina, “Two-dimensional measurements of laser-induced breakdown in air by high-speed two-frame shadowgraphy,” *Appl. Phys. A*, vol. 112, no. 1, pp. 49–55, Sep. 2012.

[13] J. O. Kokaj, “Morphological image processing of a bubble in laser-induced shock-wave lithotripsy,” in *Intelligent Systems and Smart Manufacturing*, 2000, pp. 98–106.

[14] T. McInerney and D. Terzopoulos, “Deformable models in medical image analysis,” in *Mathematical Methods in Biomedical Image Analysis, 1996., Proceedings of the Workshop on*, 1996, pp. 171–180.

[15] A. Blake and M. Isard, *Active Contours the Application of Techniques from Graphics, Vision, Control Theory and Statistics to Visual Tracking of Shapes in Motion*. London: Springer London, 1998.

[16] M. Kass, A. Witkin, and D. Terzopoulos, “Snakes: Active contour models,” *Int. J. Comput. Vis.*, vol. 1, no. 4, pp. 321–331, 1988.

[17] J. Ivins and J. Porrill, “Everything you always wanted to know about snakes (but were afraid to ask),” *Artif. Intell.*, vol. 2000, 1995.

[18] K.-M. Lam and H. Yan, “Fast greedy algorithm for active contours,” *Electron. Lett.*, vol. 30, no. 1, pp. 21–23, Jan. 1994.
[19] T. Lindeberg, “Edge detection and ridge detection with automatic scale selection,” *Int. J. Comput. Vis.*, vol. 30, no. 2, pp. 117–156, 1998.
[20] J.-M. Geusebroek, A. W. Smeulders, and J. van de Weijer, “Fast anisotropic Gauss filtering,” in *Computer Vision—ECCV 2002*, Springer, 2002, pp. 99–112.
[21] P. Radeva and J. Serrat, “Rubber snake: implementation on signed distance potential,” in *Vision Conference SWISS*, 1993, vol. 93, pp. 187–194.
[22] D. W. Scott, *Multivariate density estimation: theory, practice, and visualization*. New York: Wiley, 1992.